Eur. Phys. J. B **46**, 563–579 (2005)
DOI: 10.1140/epjb/e2005-00289-9

THE EUROPEAN PHYSICAL JOURNAL B

Properties of turbulent air avalanches in a vertical pit

F. Perrier[1,2,a], J.-L. Le Mouël[1], V. Kossobokov[3], C. Crouzeix[1], P. Morat[1], and P. Richon[2]

[1] Laboratoire de Géomagnétisme, Institut de Physique du Globe, 4, Place Jussieu, 75005 Paris, France
[2] Laboratoire Hydrogéochimie et Études de Sites, Commissariat à l'énergie atomique, B.P. 12, 91680 Bruyères-le-Châtel, France
[3] International Institute of Earthquake Prediction Theory and Mathematical Geophysics, Washavskoyeshossee 79 Korp 2, Moscow 113556, Russia

Received 5 November 2004 / Received in final form 24 May 2005

Abstract. Temperature and humidity measurements have been performed since 2000 in the atmosphere of the 20-m deep vertical access pit of an underground quarry. Air avalanches take place in the pit when the outside air density is larger than the equilibrium air density of the quarry. These avalanches are associated with a mean linear vertical temperature profile, and with broad-band, spatially organized and coherent temperature fluctuations. Temperature distributions are nearly Gaussian, with a skewness smoothly varying with position. The power spectra of the fluctuations show, in the frequency range from 3×10^{-4} Hz to 4×10^{-3} Hz, an exponent varying from -0.15 at the bottom of the pit, to -0.6 at the top. Heat exchange with the walls accounts for the mean temperature profile, and contributes to the power spectra for periods smaller than about 20 minutes. Vertical cross-correlations provide estimates of velocities and indicate quasi-stable polarization of the direction of the vertical mean flow. A horizontal vorticity index, constructed from a horizontal cross-correlation and the sign of the temperature gradient, exhibits properties of a scale-invariant process, similar to the structure of wind reversals observed in Rayleigh-Bénard laboratory convection experiments or to the reversals of the geomagnetic fields. This experiment may offer a genuine realization of bulk turbulence forced by a linear temperature gradient. More generally, it provides a description of turbulent fluid dynamics in a medium-scale natural system in the presence of non-adiabatic boundaries.

PACS. 47.27.-i Turbulent flows, convection, and heat transfer – 47.27.Sd Noise (turbulence generated) – 92.60.Ek Convection, turbulence, and diffusion

1 Introduction

Turbulent flows play an important role in natural processes [1,2], from the biological world [3] to the birth of planets [4], or the modeling of electromagnetic signals from outside our galaxy [5]. Turbulence is a key aspect of the dynamics of the Earth atmosphere [6,7], but also of most geophysical flows on the surface [8], as well as the processes of the interior of the Earth, for example the geodynamo responsible for the properties of the geomagnetic field [9–11]. Understanding the properties of turbulent fluids is also a major issue in key environmental and industrial problems of the new century, such as the dispersion of pollutants [12], the spread of epidemics [13], or the initiation of inertial confinement fusion [14]. In all these various domains, turbulence often exhibits common and surprisingly simple features, with patterns of organization that can be accounted for by scaling laws relying on dimensional arguments [1,2]. While the conservation of fundamental quantities provides a sound basis in most cases for some basic observations [15], a detailed theoretical understanding of the properties of turbulent flows and their consequences remains a fascinating challenge of the mathematical and physical sciences [1].

Most of the fundamental studies still rely on model experiments performed in well-controlled laboratory conditions such as wind tunnels [15], dye jets experiments [16], Hele-Shaw cells [17] and Rayleigh-Bénard [18] (RB) convection, where a fluid container is heated from below and cooled from above. Turbulent RB convection experiments deserve particular attention because they are particularly relevant for the understanding of confined and semi-confined geophysical flows with low Reynolds numbers *Re*. In addition, RB experiments have been fruitful in unraveling many features of turbulent dynamics such as coherent structures [19], oscillations and intermittent fluctuations [20,21] as well as anomalous scaling [22].

The coherent large-scale circulation (LSC) motion [19], also referred to as the mean wind, is observed to arise, superimposed on the background turbulence, when the forcing parameter, the Rayleigh number *Ra*, is increased above about 10^6. This coherent large-scale rotation has now been studied in RB cells with various fluids including, for example, helium gas [23] or in water using Laser-Doppler velocimetry techniques [21]. Although recent

---

[a] e-mail: perrier@ipgp.jussieu.fr

numerical modeling confirms the existence of large scale structures creating a mean flow sweeping the sides of the box [24], the origin of the wind remains debated. Oscillations and intermittent fluctuations, which are also an important property of RB convection, result from the interaction between the LSC and thermal plumes [25,26]. A mechanism, where sheared thermal plumes are initiating the LSC, is supported by a detailed study of velocity fluctuations and temperature-velocity cross-correlations [27], complemented by further imagery techniques [28]. However, other mechanisms are also proposed [29].

One of the most unexpected properties of the LSC is the stochastic structure of reversals in the direction of motion. These reversals had been noticed in several experiments, but have been studied for the first time in cryogenic helium gas at high Rayleigh number, in a cell of aspect-ratio 1 [23]. While a Brownian-type process is indicated by an exponent -2 of the power spectrum, the observed distribution of the time intervals between reversals also suggests a hierarchical structure with exponent -1, pointing to self-organized critical phenomena [8]. These properties of the reversals are particularly interesting to study as they bear a striking similarity to the dynamics of reversals of wind directions [6], and of the inversions of the geomagnetic field [30,31].

Exponents of the frequency dependence of the power spectra are also important parameters of temperature and velocity fluctuations, and of the temperature-velocity cross-correlations as well. Dimensional arguments [1,15], assuming energy cascades with scale-independent entropy flux, provide a power law with slope $-11/5$ for the velocity fluctuations and $-7/5$ for the temperature fluctuations (Bolgiano-Obukhov [32] or BO scaling). In contrast, the assumption of a constant energy flux leads to a slope of $-5/3$ for both the velocity and temperature spectra (Kolmogorov scaling or KO) [33,15]. KO scaling has been observed in wind tunnel experiments over three decades of frequency [15]. In RB experiments, the situation is more complex. BO scaling is observed in the velocity and temperature power spectra in helium gas [34], in SF6 [35] or mercury [36]. In water [22], BO scaling is observed above the peak frequency f_p of the dissipation spectrum $f^2P(f)$. Below this characteristic frequency f_p, an anomalous exponent -1.35 is observed [22]. Numerical modeling [24] yields BO scaling for the temperature spectrum, but leads to KO scaling for the velocity spectrum.

Despite these open questions, a globally consistent picture of turbulent RB convection has emerged [37], and unified scaling laws have been derived for example for the Re and Nusselt numbers Nu versus Ra. It may be noted that experimental values of the scaling parameters still remain to be clarified, in particular because of still incompletely known geometrical effects [38]. In any case, the general applicability of these scaling laws to other turbulent systems is not straightforward. Features of RB convection, such as the existence of the LSC and its fluctuations, the slopes of the power spectra, the presence of interactions between large-scale flow and plumes, may not be universal properties of turbulent convection in general. In order to investigate this question, different types of well-controlled experiments beyond the laboratory scale are of great interest.

In a first paper [39], we have described the properties of temperature records observed in a medium-scale natural system: the access pit of an underground quarry. This system is a vertical cylinder of 4.56 m diameter and height 20 m, largely open to the outside atmosphere. Half of the year, as long as the outside air density is larger than the equilibrium density of the quarry air, avalanches take place in the pit [39], producing natural ventilation of the whole quarry. The presence of this natural ventilation is confirmed by the seasonal variation of the radon concentration [40], which indicates ventilation rates varying from 0.5 to 4×10^{-6} s^{-1}, corresponding to averaged volumetric flow rates varying from 0.03 to 0.24 m^3 s^{-1}. The onset of air avalanches in the pit is associated with broad-band temperature fluctuations. The standard deviation of the fluctuations is proportional to the temperature difference between the upper part of the pit and the equilibrium temperature of the quarry [39]. In addition, these temperature fluctuations are coherent on a vertical profile.

In the present paper, using an improved experimental set-up and a comprehensive data set, we elaborate in details on the preliminary observations, we present new results, and we discuss the nature of the turbulent flows observed in the pit. In the following, the setting and the instruments are first described. Time series of temperature and humidity are then introduced to outline the working modes of the system. After the averaged properties are presented, we turn to a discussion of the probability distribution functions (PDF) and power spectra. Vertical correlations are presented and lead to estimates of vertical velocities. The analysis of horizontal correlations provides a way to capture the stochastic nature of the turbulent flow structures, in particular flow reversals. At the end of the paper, we present a discussion of these various properties in the light of RB convection and general turbulence. The consequences of the turbulent flows taking place in the pit in terms of the energy and composition budget of the whole quarry, or the role of phase changes of water are outside the scope of the present paper.

2 The site and the experimental set-up

The abandoned "La Brasserie" limestone quarry is located under the park of Vincennes near Paris. It consists of pillars and rooms with a height varying from 2 m to more than 4 m excavated in Lutetian limestone, 18 m below ground surface [41]. The total air volume V_{tot} in the quarry is estimated to be around 60 000 m^3. The temperature in most of the quarry is stable, with an average value of 12.7 °C and yearly variations of the order of 0.16 °C in the atmosphere and 0.2 °C in the rock [42]. The relative humidity RH is larger than 99.8% in non-ventilated conditions, and varies from 99.2 to 99.8% during ventilated conditions in winter. Water vapor saturation of the quarry atmosphere is maintained by water drippings.

The quarry is connected to the ground surface by a single large access pit (Fig. 1) with 4.56 m diameter (D). This pit of height $h = 20$ m can thus be considered as a vertical pipe linking the outside atmosphere, where temperature and RH vary on daily and seasonal cycles, to a finite but large volume of air V_{tot} at 12.7 °C and 100% RH. All other known ventilation pits of the quarry are now sealed. Unexplored galleries are present but they are not expected to contribute to the natural ventilation. Air exchange is thus expected to proceed through the main access pit only. This pit dates back to the creation of the quarry in the eighteenth century. It was reopened in 1989 to install a metallic staircase, now used to enter the quarry (Fig. 1). This metallic staircase of diameter about 2.2 m slightly obstructs the air flow, leaving a free area S_{eff} of 15.4 m^2 in the pit. The upper part of the pit reaches in a building, but broken panes in windows with a surface area of about $S_w = 2.3$ m^2 allow air exchange with the outside atmosphere.

Measurements in the pit are performed along vertical and horizontal profiles (Fig. 1). In an initial phase, from the beginning of 2000 to the beginning of 2003, a vertical profile of 10 temperature measurements located near the staircase was used [39]. In October 2001, a new vertical profile was installed (Fig. 1). This profile, located about 65 cm from the staircase (Fig. 1), consists in 10 points separated by 1.75 m. At each point, one temperature measurement and one relative humidity measurement are performed. Temperature measurements, labeled from TV1 to TV10 (Fig. 1), are performed using the same thermistor type as the first vertical profile [39]. This thermistor has a diameter of 5 mm, a length of 30 mm and a resistance R to temperature T relationship that can be approximated for our present purpose by an exponential function $R = R_0 \exp(-T/T_0)$ with $R_0 = 5700\ \Omega$ and $T_0 = 27$ °C. The sensitivity is then about $150\ \Omega\ {}^\circ\mathrm{C}^{-1}$ at 10 °C and $100\ \Omega\ {}^\circ\mathrm{C}^{-1}$ at 20 °C. The absolute calibration has been determined in a thermal bath with an accuracy of 0.1 °C. Because of their finite size, the thermistors have a response time of the order of 30 seconds.

Relative humidity measurements, labeled from RHV1 to RHV10 (Fig. 1), are performed using semi-conductor detector chips protected by porous pots with 12 mm diameter and 25 mm length. This probe has a strongly nonlinear response R to RH, approximated by an ad-hoc analytical function. The parameters of this function have been determined using dedicated calibration runs in a climatic chamber [43]. Because of the diffusion of air through the porous pot, this sensor has a characteristic response time of the order of 15 minutes, determined in the climatic chamber with similar sensors.

The vertical temperature profile was complemented in March 2004 by a horizontal profile of five thermistors, labeled BH1 to BH5, located about 4.1 m below ground surface (Fig. 1). These thermistors are of the same type as the vertical profile. In addition, in order to sample the temperature variations in varying places of the pit volume, a movable set-up was installed in September 2001. This set-up (Fig. 1) consists in four branches of five thermistors each, with a regular spacing of 18 cm. Three branches are located at the same level, and the fourth branch, 1.3 m below, as indicated in Figure 1. The position of the set-up was changed during 2002 and, in September 2003, it was placed in the configuration indicated in Figure 1. Winter data of the movable set-up discussed in this paper refer to this latter position. The thermistors of this movable set-up are of a different type, with the shape of a square with a thickness of 0.7 mm and a width of 8 mm, pierced by a 3.8 mm diameter hole. Their parameters have been determined in a calibration bath, and follow the relationship $R = R_0 \exp(-T/T_0)$ with values $R_0 = 28000\ \Omega$ and $T_0 = 24$ °C [43]. Their sensitivity is about $780\ \Omega\ {}^\circ\mathrm{C}^{-1}$ at 10 °C and $500\ \Omega\ {}^\circ\mathrm{C}^{-1}$ at 20 °C. Their smaller mass offers the advantage of a response time of the order of 10 seconds. The windows at the top of the pit are located just above the movable set-up (Fig. 1), whereas the vertical profile hangs on the opposite side of the pit with respect to the windows.

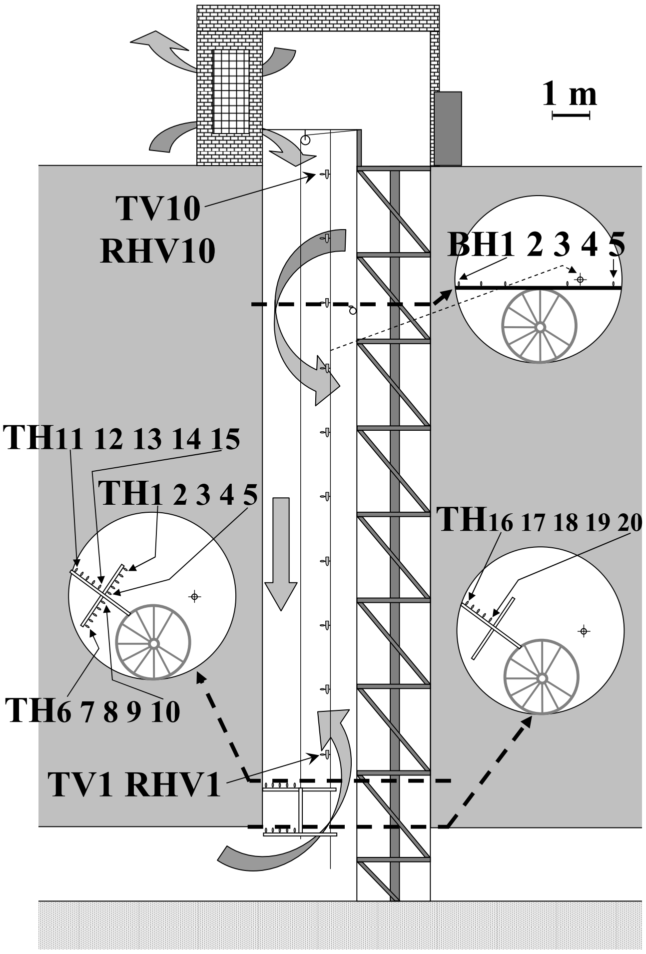

Fig. 1. Access pit of the Vincennes quarry, showing the location of the instruments. Temperature measurements are performed along a vertical profile: TV1 to TV10 from bottom to top, along with relative humidity measurements RHV1 to RHV10. Horizontal temperature profiles are also available in the upper part of the pit (BH1 to BH5) and on the four branches of the movable set-up (TH1 to TH20). The shaded arrows sketch the mean direction of the air flow.

In addition to the temperature and humidity measurements, atmospheric pressure variations are recorded in the upper part of the pit, together with the pressure difference between the top and the bottom of the pit. The outside temperature has been recorded since September 2003 with autonomous Tinytag$^{\mathrm{TM}}$ recorders located under the roof, above the entrance door of the quarry pit. The vertical profile has been operated without interruption and the movable set-up with 95% efficiency since October 2001, with sampling intervals varying from 10 s to 2 min. Continuous operation of the instruments is guaranteed by a battery buffer in case of failure of the AC power. The horizontal profile has been operated since March 2004, with 1 minute sampling interval.

3 Observations from the temperature time series

Temperatures recorded with the vertical profile during the initiation phase of the natural ventilation in autumn are shown in Figure 2. The temperature in the lower part of the pit is stable (TV1 and TV2 for example) as long as the outside temperature and relative humidity remain such that the outside air density is larger than the equilibrium air density in the quarry. In this summer regime, the temperature in the upper part of the pit (sensor TV10) is similar to the external temperature, or slightly smaller. Heat exchange between the pit and the outside then proceeds essentially by diffusion, with possible transient episodes of wind. In addition, the effect of atmospheric pressure variations can be seen. For example, a pressure increase occurs in the evening of September 22. This pressure increase is associated with a clear temperature wave traveling down to the bottom of the pit, with amplitude of the order of 1 °C peak to peak at sensor TV1. This wave corresponds to hot air pushed into the quarry. In contrast, pressure decreases, even with large amplitude, or, more significantly, large time derivative, have no measured effect larger than 0.1 °C on TV1 and TV2. In this case, indeed, air at the stable temperature of the quarry is dragged across the sensor. Smaller effects of the pressure variations could however still be observed at a finer temperature scale [44]. Notice that the thermal effects of small atmospheric pressure variations can be easily observed from sensors TV7 to TV10 during summer regime. This part of the pit behaves then as an amplifier of atmospheric pressure variations, due to the large volume of the quarry pushed and pulled through the pit (cave breathing effect [45]).

When the air avalanches are triggered in the pit, a different behavior of the temperature is observed (Fig. 2b). Fluctuations of the order of 1 °C peak to peak are noticed on all sensors, sometimes with transient spikes at the beginning of the night, confirming the observations with the first vertical profile [39]. Figure 2b also indicates that, during air avalanches, the temperature in the upper part of the pit (TV10) is almost the average between the outside temperature and the equilibrium quarry temperature. This fact reflects the vigorous mixing of the air in the pit during the avalanches, which is also associated with a slightly negative pressure difference (Fig. 2a).

The temperature evolution of the pit is shown in Figure 3 for longer time scales. In this figure, the temperatures have been averaged over sliding time windows of 30 minutes duration and the standard deviation of data during the same window has been plotted separately (Fig. 3b). The initiation of avalanches is associated with a temperature drop in the whole pit and the standard deviation of the fluctuations increases linearly with the temperature change as previously observed with the first vertical profile [39]. When the temperature in the pit is increasing, the amplitude of the temperature fluctuations is simultaneously decreasing, as, for example, during the fair days of 16 to 18 December 2003. During persistence of cold weather, however, constant average temperature and size of the fluctuations are maintained over several days.

The behavior of relative humidity is also shown in Figure 3c. Outside air is cold and dry compared with the air of the pit. Consequently, air avalanches induce a desaturation of the atmosphere of the pit and a dry front travels slowly down the pit, for example from December 14 to 15 (Fig. 3c), with a velocity of about 1 m per hour. The presence of non-saturated air in the pit induces evaporation from the wall and can in principle induce a thermal feedback response [39]. Non-saturated conditions, however, are not maintained over long periods of time. As soon as the temperature recovers, even in a cyclic manner as during the day from 16 to 18 December 2003, the relative humidity is restored to values larger than 99%, which indicates that evaporation occurs, even though the temperature is rising in the pit. In addition, during the desaturated phase, intriguing coherent oscillations of RH are observed on sensors RHV8, RHV9 and RHV10. These data suggest that natural ventilation induces a complex dynamics of evaporation and condensation, with several possible stationary mixing states with different properties.

The peculiar thermal dynamics of the pit is also seen when considering long time periods. In Figure 4a, the distribution of the hourly averaged temperature difference between TV10 and TV1 is shown. The summer regime is characterized by large positive excursions of this temperature difference, whereas the ventilated winter regime is characterized by a strong constraint of the temperature difference, maintained as a peaked distribution with an average value of −1.6 °C.

The distribution of temperature difference, when negative, can be translated into a Rayleigh number distribution (Fig. 4b). In this case, let us define Ra as:

$$Ra = \frac{g\alpha \Delta T h^3}{\nu\kappa}, \tag{1}$$

where g is the acceleration of gravity, α the volumetric thermal expansion coefficient of air (3.4×10^{-3} K^{-1}), ν the air kinematic viscosity (1.5×10^{-5} m^2 s^{-1} at 13 °C), κ the thermal diffusivity of air (1.9×10^{-5} m^2 s^{-1}), and ΔT the temperature difference between the bottom and the top of the pit. The latter quantity is estimated as $\Delta T = (T_{\mathrm{TV1}} - T_{\mathrm{TV10}})/(z_1 - z_{10})^* h$, where $T_{\mathrm{TV1}} - T_{\mathrm{TV10}}$

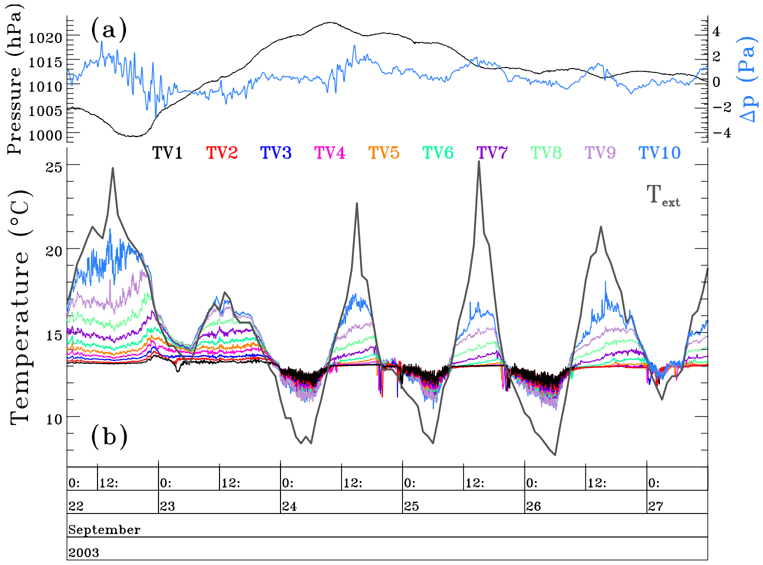

Fig. 2. Atmospheric pressure and pressure difference (a) and temperature time series (b) recorded with the vertical profile TV1-10 from 22 to 27 September 2003. Sampling interval is 2 min. The atmospheric pressure is recorded in the pit at surface level. Pressure difference is the pressure at the top minus the pressure at the bottom of the pit. The outside temperature T_{ext} included in (b) is recorded under the roof above the entrance door with a sampling interval of 1 hour.

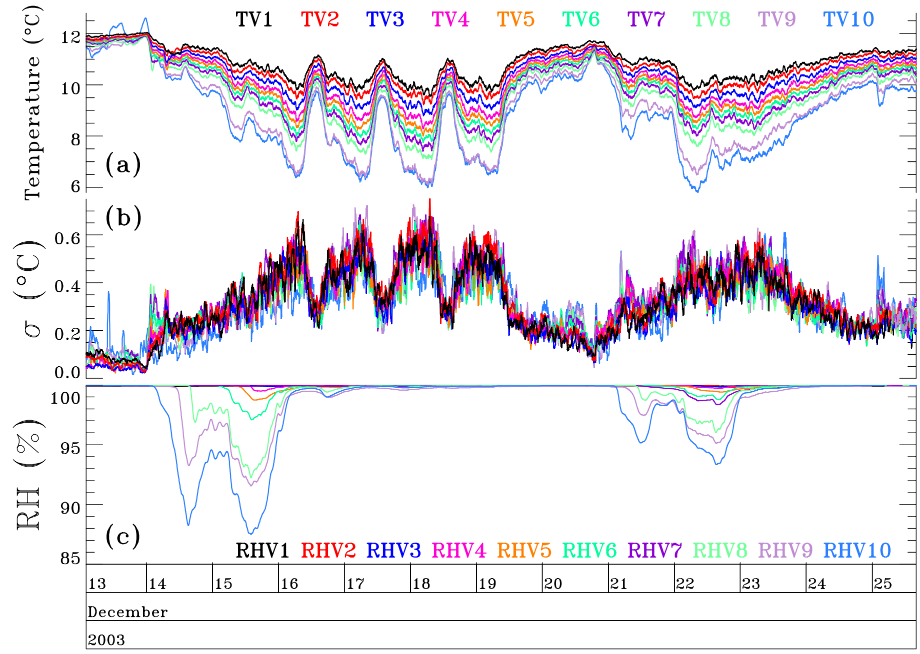

Fig. 3. Mean temperature (a), standard deviation (b) and relative humidity (c) recorded with the vertical profile TV1-10 and RHV1-10 in December 2003. Mean and standard deviations are calculated using 30 minutes long moving windows.

is the measured averaged temperature difference between sensors TV1 and TV10 (1.6 °C from Fig. 4a) and z_i the vertical position of sensor TVi. The mean value of ΔT is then 1.8 °C.

The average Ra number over one season of ventilation (Fig. 4b) is about 10^{12}. If the scaling laws of RB cells are applied [37], namely $Nu = 0.22\ Ra^{0.289}$ and $Re = 3.5\ Ra^{0.446}$, this value implies $Nu = 650$ and $Re = 7.9 \times 10^5$. Although these scaling laws do not strictly apply to our regime ($Ra \sim 10^{12}$), these estimates appear reasonable. In RB cells, Re is defined as Vh/ν, where V is a typical large-scale velocity. This relation gives then $V = 60\ \mathrm{cm\,s^{-1}}$. The thickness of the sidewall boundary layer δ can also be estimated using $\delta/h = 3.6\, Ra^{-0.26}$ derived from RB experiments in water [46] and we obtain 5.5 cm.

Typical velocities in the pit can also be estimated from the values of the ventilation rate obtained from the

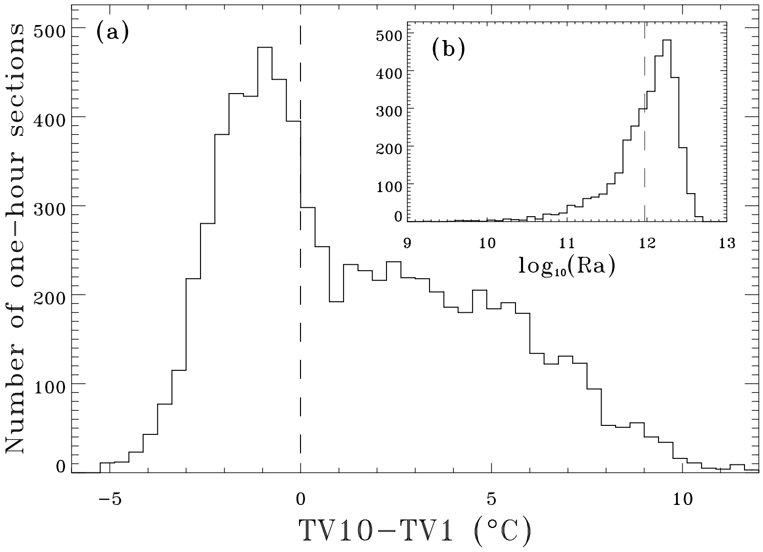

Fig. 4. (a) Distribution of temperature difference $T_{\mathrm{TV10}} - T_{\mathrm{TV1}}$ for hourly averages from October 2001 to October 2002. (b) Corresponding distribution of Rayleigh number *Ra* when temperature difference $T_{\mathrm{TV10}} - T_{\mathrm{TV1}}$ is negative (winter regime).

seasonal variation of the radon concentration [40]. The measured ventilation rate depends on the position in the quarry, with values 0.5×10^{-6} s^{-1} in the least ventilated zone, 2×10^{-6} s^{-1} in open rooms, and 4×10^{-6} s^{-1} at the bottom of the pit. Attributing a volume of 20 000 m^3 to each of these sensors, the time-averaged total volumetric flow rate of the quarry is estimated to be 0.13 m^3 s^{-1}. Assuming that this flow takes place through half of the effective area S_{eff} of the pit, the corresponding mean velocity is then of the order of 2 cm s^{-1}. This estimate, albeit uncertain, is significantly smaller than the value obtained previously from the Rayleigh number and RB scaling laws. Even with $V = 2$ cm s^{-1}, the corresponding *Re*, defined here as $Re = VD/\nu$, amounts to 6000; thus we can infer that the flow definitely takes place in a turbulent regime.

The average heat flux F_C transported by the convective motion, corresponding to the mean ventilation rate of the quarry, can be estimated as:

$$F_C = \rho c_p \frac{S_{\mathit{eff}}}{2} \Delta T \, V, \tag{2}$$

where ρ and c_p are the density and the specific heat capacity of air, respectively. Taking $\rho = 1.2$ kg m^{-3}, $c_p = 10^3$ J kg^{-1} °C^{-1}, $\Delta T = 1.8$ °C and $V = 2$ cm s^{-1}, we obtain $F_C = 333$ W. Another estimate will be obtained from the horizontal temperature distributions in Section 8.

4 Properties of time average quantities

Before describing the properties of the temperature fluctuations in the pit in more details, we present in this section the spatial properties of time averaged quantities, concentrating on the average temperature and the standard deviation. Average temperature profiles are shown in Figure 5 for various time periods. In this paper, the vertical coordinate z in the pit is taken positive upwards, with $z = 0$ at ground surface. In summer, an exponential temperature profile $e^{z/\lambda}$ is observed, with a characteristic length λ varying between 5 and 10 m. The attenuation length of the harmonic of period t is given by: $\sqrt{\kappa t/\pi}$, which gives 14 m for annual waves. The observed profile is therefore controlled by diffusion in summer. In contrast, when air avalanches occur in the pit, as illustrated by the data of the night from September 22 to 23 (Fig. 5), a different vertical temperature profile is observed, almost linear from top to bottom. This linear profile is present during the whole winter regime. Transition periods are observed in May 2003, September 2003 and April 2004. In the following, we will be dealing with the winter regime only.

The temperature profiles observed in winter in the pit depend on the forcing, which is proportional to the mean temperature difference $T_0 - T_{\mathrm{TV10}}$ between the equilibrium quarry temperature T_0 (12.7 °C) and the temperature measured at the top of the pit T_{TV10}. A reduced temperature thus can be defined as:

$$\theta(t) = \frac{T_0 - T(t)}{T_0 - \langle T_{\mathrm{TV10}} \rangle}, \tag{3}$$

where $\langle T_{\mathrm{TV10}} \rangle$ is the average value of T_{TV10} and is calculated over time portions of 200 data points.

The average value of θ and its standard deviation σ_θ are shown in Figure 6 as a function of the vertical position z in the pit, showing the results of independent time sections. A remarkable linear variation of θ is observed as a function of the vertical position, independent of time, hence independent of the forcing from atmospheric conditions. This profile thus reflects an intrinsic mixing response of the pit. Extrapolation to the bottom of the pit leads to values θ_0 of 0.39 ± 0.02. This suggests that a significant fraction of the mixing takes place outside of the pit, in the quarry itself. Air avalanches reach the bottom of the pit and, with a mechanism similar to a filling box [47], fill the entire quarry [40]. This observation is

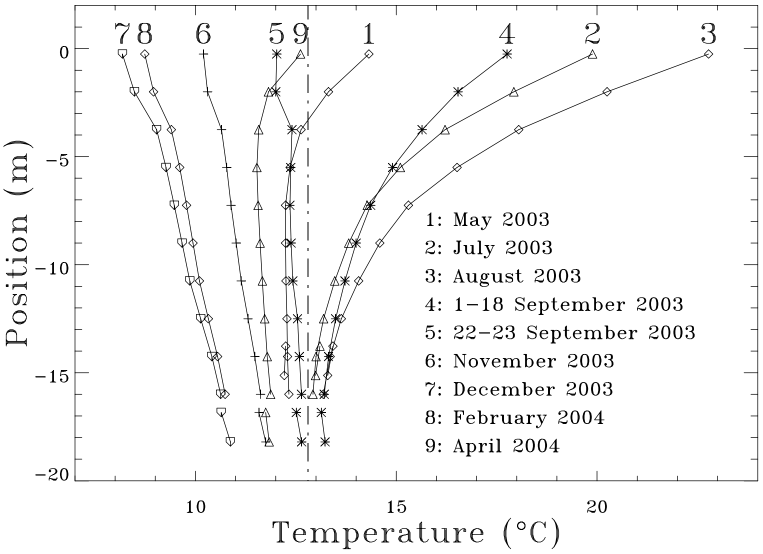

Fig. 5. Vertical temperature profile in the pit averaged over the indicated time periods.

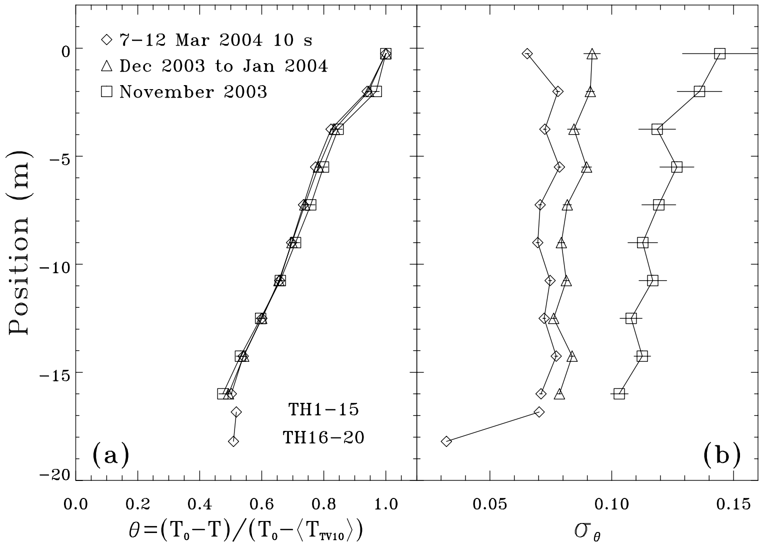

Fig. 6. Average reduced temperature (a) and its standard deviation (b) versus vertical position in the pit. Reduced temperature is defined as $\theta = (T_0 - T)/(T_0 - \langle T_{\mathrm{TV10}} \rangle)$, where T_0 is the equilibrium quarry temperature (12.7 °C) and $\langle T_{\mathrm{TV10}} \rangle$ is an average temperature measured with sensor TV10.

confirmed by measurements of radon concentration [40], temperature [42] and humidity in the quarry.

The observed slope of $\theta(z)$ translates to a mean vertical temperature gradient of about -0.1 °C m^{-1}. This value can be compared with the adiabatic gradient:

$$\frac{\partial T}{\partial z} = -\frac{\alpha g T_K}{c_p}, \tag{4}$$

where T_K is the absolute temperature. The value of the adiabatic gradient is thus -0.01 °C m^{-1}, about ten times smaller than the observed gradient. The mixing in the pit thus differs significantly from the conditions of a RB experiment where a near-adiabatic gradient is observed in the volume of the cell, with most of the temperature gradient taking place in the boundary layers [20,46].

The mean heat flux exchanged with the wall F_W can be estimated using the observed temperature profiles. For a vertical temperature difference ΔT, as defined in equation (1) (Sect. 3), the temperature is given as a function of z by:

$$T(z) = T_0 - \Delta T \left(\frac{1}{1-\theta_0} + \frac{z}{h} \right), \tag{5}$$

and we have:

$$F_W = \pi R \beta \int_{-h}^{0} \left(T_r(z) - T(z) \right) dz, \tag{6}$$

where R is the radius of the pit, $T_r(z)$ the temperature of the wall and β the heat conductance at the wall. Here we assume that the pit is a perfect cylinder and we neglect the presence of the staircase. The conductance β is related to the characteristic thermal relaxation time τ defined by:

$$\frac{2\beta}{\rho c_p R} = \frac{1}{\tau}. \tag{7}$$

The relaxation time τ can be estimated from pressure induced temperature variation and is of the order of 26 minutes [44], corresponding to $\beta = 0.8$ W m^{-2} °C^{-1}. From equations (5–6), assuming $T_r = T_0$, we have:

$$F_W = F_W^0 = \pi R \beta h \Delta T \frac{1+\theta_0}{2(1-\theta_0)}, \tag{8}$$

which, for $\Delta T = 1.8$ °C, gives $F_W^0 = 235$ W, smaller but of the same order of magnitude as F_C. Note that the rock surface must reach equilibrium with the air mass, so that the estimate given by equation (8) is actually an upper limit of F_W. The time variation of $T_r(z)$ due to vertical heat diffusion from the ground surface can actually be taken into account in a numerical model. The result remains the same within 5%, except at the beginning and end of the winter.

The ratio of F_W to F_C, a Stanton number, can be bounded by:

$$St = \frac{F_W}{F_C} \leq \frac{F_W^0}{F_C} = \frac{h}{\tau V} \frac{1+\theta_0}{2(1-\theta_0)}. \tag{9}$$

For $V = 60$ cm s^{-1}, $St = 0.02$ and the heat exchange with the wall is negligible compared with the convective heat flux. In our system, these estimates thus indicate that fast transport processes, with velocities of the order of 20 cm s^{-1} or larger can be considered as adiabatic, whereas slow transport processes characterized with velocities close to the mean velocity 2 cm s^{-1} are partly controlled by temperature exchange with the walls.

The origin of the linear vertical temperature profile and the magnitude of the slope can be understood with the following simple argument. Let us assume that a downward flow of air takes place in one half of the pit, with velocity $-V$ and temperature $T_-(z)$, and that an upward flow of air takes place in the other half of the pit, with velocity $+V$ and temperature $T_+(z) = T_0$, the mean temperature of the quarry. In addition, let us assume that the downward air flow is in thermal equilibrium with the wall at temperature T_0, which, on average, implies:

$$\frac{\partial T_-}{\partial t} = 0 = V \frac{\partial T_-}{\partial z} - \frac{1}{\tau}(T_- - T_0). \tag{10}$$

The solution is:

$$T_-(z) = T_0 + (T_{ext} - T_0) e^{\frac{z}{\lambda_W}}, \tag{11}$$

where T_{ext} is the external temperature and $\lambda_W = V\tau$. If we now assume that the observed temperature corresponds to a full mixing, at each z, between the downward and the upward air flow, then:

$$T(z) = \frac{1}{2}\left(T_+(z) + T_-(z)\right) = T_0 + \frac{(T_{ext} - T_0)}{2} e^{\frac{z}{\lambda_W}}. \tag{12}$$

For $V = 2$ cm s^{-1} and $\tau = 26$ min, we have $\lambda_W = 31$ m and the exponential profile given by equation (12) is almost linear for $-h < z < 0$. From equation (12), we also predict $\theta_0 = \exp(-h/\lambda_W) = 0.52$, which is in satisfactory agreement with the observed value $\theta_0 = 0.39 \pm 0.02$. This model is however simplistic and substantial recirculation of the flow must occur with turbulent mixing, associated with fragmentation of the most rapid eddies into turbulent cascades down to the dissipation scale. Describing the physics behind the temperature profile thus requires more information about the turbulent structure of this system.

In a first approximation, the standard deviation σ_θ (Fig. 6b) is independent of the position in the pit, and is also approximately independent of time, with a characteristic value varying from 0.08 to 0.1. A repeatable spatial structure is however noticed in Figure 6b, with increased relative fluctuations at the level of sensor TV7 or TV2. In Figure 6, data from the movable set-up are also included for comparison. Averaged values of θ are significantly larger for these sensors compared with the values extrapolated from the vertical profile at the position of the movable set-up (Fig. 6a). The value of σ_θ is smaller for the lower branch of the set-up than for the higher branch (Fig. 6b). This must be due to the fact that this lower branch is not in the pit, but dips in the atmosphere of the quarry (Fig. 1). In principle, the difference between the vertical profile and the sensors of the movable set-up in Figure 6 could be due to an inappropriate intercalibration between the two thermistor types. This intercalibration was performed in July 2003 when the movable set-up was at a higher position (Fig. 5). The difference in terms of temperature observed in winter in Figure 6a would need to be of the order of 0.2 °C, which is incompatible with the expected precision of the intercalibration (0.05 °C). Another explanation has to be proposed. In fact, the sensors of the movable set-up are located from 2 m to 3 m away from the vertical profile (Fig. 1). Large horizontal variations of $\langle\theta\rangle$ and σ_θ in winter could explain the observed shifts. A smooth variation is indeed confirmed using the data of the horizontal set-up TH (Fig. 1), superimposed to an overall remarkably uniform horizontal distribution. Therefore, the shifts indicated in Figure 6b are probably genuine.

Spatial variations of averaged quantities thus indicate that, despite the turbulent mixing processes, a definite spatial organization is maintained. At this stage, it is not known whether such structures are maintained over long periods of time and whether substructures could also survive for some shorter periods of time. Such privileged structures could be imposed by the boundary conditions, for example the fact that windows are only present on one side of the building (Fig. 1) or the fact that most of the volume of the quarry at the bottom of the pit is located west of the pit, on the side of the movable set-up. The structures could also be constrained by the heterogeneous structure of the pit itself, characterized by the presence of the staircase.

The fact that persistent structures can be imposed by boundary conditions appears to be a general feature of

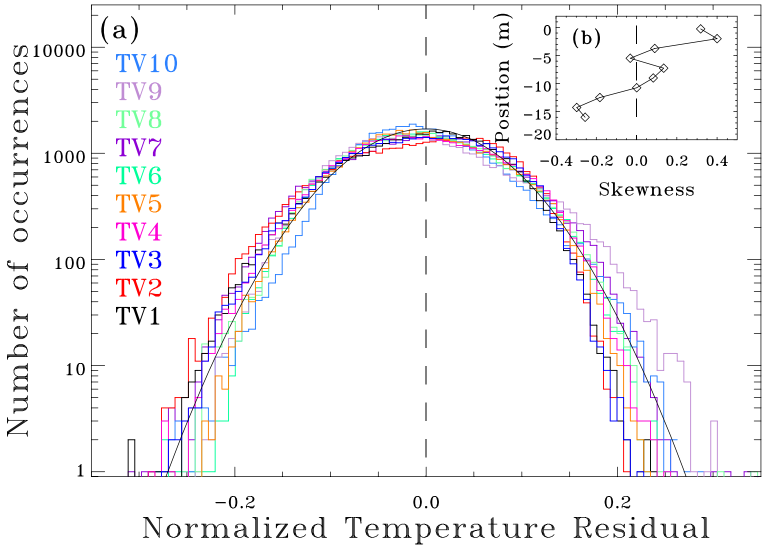

Fig. 7. (a) Distribution of normalized temperature residuals for the vertical set-up recorded from 7 to 12 March 2004 (sampling 10 s, total of 41 000 data points). Normalized temperature residuals are defined as $\theta_r(t) = (T - T_L(t))/(T_0 - \langle T_{\rm TV10}\rangle)$, where T_0 is the equilibrium quarry temperature (12.7 °C), $\langle T_{\rm TV10}\rangle$ is an average temperature measured with sensor TV10, and $T_L(t)$ is a fitted linear trend over portions of 200 data points. The black line corresponds to a Gaussian distribution with standard deviation 0.07. (b) Inset: skewness of distribution versus position in the pit.

natural turbulent systems. For example, it has been proposed that convection in the inner earth core exhibits horizontal patterns persisting over time scales much larger than the circulation times [48]. Inversions of the geomagnetic field also have been claimed to have preferred azimuthal pathways [49]. Such structures, if genuine, are proposed to be imposed by the core-mantle boundary [50]. Persistent patterns may have important consequences in other contexts, such as the creation of ecological niches or increased sedimentation in river flows [51]. Further spatial organization of the pit turbulence is identified in the next section with the properties of the temperature PDF and power spectra.

5 Temperature probability distributions and power spectra

Probability distributions of the normalized temperature residuals defined as:

$$\theta_r(t) = \frac{T(t) - T_L(t)}{T_0 - \langle T_{\rm TV10}\rangle}, \qquad (13)$$

where T_L is the temperature trend obtained from a linear fit over a portion of 200 data points, are presented in Figure 7a. In a first approximation, these PDFs are Gaussian and similar along the vertical direction, with a standard deviation σ of about 0.07. The latter fact was indicated already by the uniform σ_θ as a function of z (Fig. 6b). Looking more closely, these distributions however are skewed. The skewness, defined as $\langle\theta_r^3\rangle/(\langle\theta_r^2\rangle)^{3/2}$, exhibits a smooth variation as a function of z (Fig. 7b), with local anomalies for sensors TV2 and TV7, as already noticed in Figure 6b. Negative skewness in the lower part of the pit indicates more frequent small hot plumes. In contrast, the upper part of the pit is dominated by small cold plumes. The middle part of the pit is characterized by small skewness and thus comparable abundance of hot and cold plumes of similar size.

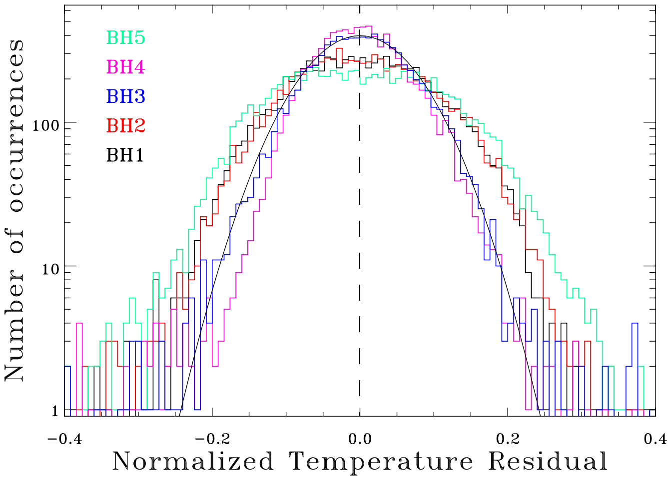

Fig. 8. Distribution of normalized temperature residuals for the horizontal set-up BH1 to BH5 recorded from 21 to 27 March 2004 (sampling 1 min). Normalized temperature residuals are defined as $\theta_r(t) = (T - T_L(t))/(T_0 - \langle T_{\rm TV10}\rangle)$, where T_0 is the equilibrium quarry temperature (12.7 °C), $\langle T_{\rm TV10}\rangle$ is an average temperature measured with sensor TV10, and $T_L(t)$ is a fitted linear trend over portions of 200 data points. The black line corresponds to a Gaussian distribution with standard deviation 0.07.

PDFs of normalized temperature residuals from the horizontal profile (sensors BH1 to BH5 in Fig. 1) are presented in Figure 8. In this case, the PDFs are roughly Gaussian with the presence of additional tails, which may be accounted for by another Gaussian part with a larger standard deviation. Three groups of sensors can be distinguished in Figure 8: sensors BH1-BH2 ($\sigma = 0.10$), sensors BH3-BH4 ($\sigma = 0.08$), and sensor BH5 which has a significantly larger standard deviation ($\sigma = 0.12$). The skewness varies from -0.9 (BH3) to 0.3 (BH4).

Gaussian PDFs are familiar in RB experiments for the velocity distributions [35], with a skewness depending on the position in the cell [25]. However, temperature distributions [20] are reported to be Gaussian at low Ra ($Ra < 4 \times 10^7$) while, in the hard turbulence regime ($Ra > 4 \times 10^7$), temperature distributions exhibit a scale-free (power-law) character [20]. This suggests that rather different processes operate in the quarry pit compared with RB cells. Furthermore, in our case, the standard deviation varies linearly with the temperature forcing [39], hence linearly with Ra. In the hard turbulence regime of RB cells [20,23], the standard deviation of the temperature fluctuations scales with Ra as $Ra^{-0.15}$.

One tentative explanation may however be proposed from the results of a RB experiment with water performed with an obstructed sidewall [52]. This situation, in contrast to a smooth RB cell, corresponds to the presence of obstacles sticking out of the sidewall, thus distorting the LSC [52]. In this case, a PDF composed of the addition of two separate Gaussian curves is observed, while power-law PDFs are observed without obstruction with the same Ra scaling as observed in helium [20]. Furthermore, larger standard deviations are observed with obstruction [52], with a different scaling law: $Ra^{-0.24}$. This experiment suggests that the functional form of the PDF reflects the flow pattern in the cell [52]. In the case of the quarry pit, the metallic staircase may play the role of an obstruction which would constrain the flow patterns, as already suggested from the spatial variations of the averaged quantities. The staircase thus would restrict or fragment the larger cascades.

Another contribution to this discussion may come from an experimental study of the temporal fluctuations of the total power injected in a swirling flow between two coaxial counter rotating disks [53]. The statistical properties of the PDF of the power fluctuations were observed to be qualitatively different for shrouded flow (non-Gaussian PDF) and free geometry (almost Gaussian) [53]. In this case, free geometry corresponds to the two disks rotating in air, whereas the shrouded geometry corresponds to the situation where the disks are enclosed in a cylindrical vessel. This result also suggests that the statistical properties of the turbulent fluctuations are related to the confinement of the flow. Two factors thus may contribute to the nearly Gaussian distributions we observed in the pit: presence of obstruction and open flow geometries at the top and bottom.

The temperature power spectra are shown in Figure 9a versus frequency f for the vertical profile. The various spectra are similar and show three frequency domains. The high frequency region ($f > 5 \times 10^{-3}$ Hz) is dominated by the filtering effect due to the finite size of the thermistors. From 3×10^{-4} Hz to 4×10^{-3} Hz, a nearly flat spectrum is observed. This is the region dominated by the temperature fluctuations associated with the air avalanches, as indicated by the different spectrum observed during summer regime (Fig. 9a). When a power-law fit is performed in the frequency range from 3×10^{-4} Hz to 4×10^{-3} Hz, exponents vary from -0.14 ± 0.04 at the bottom of the pit to -0.61 ± 0.05 at the top of the pit, with a smooth variation in between (Fig. 9c). For frequencies smaller than 2×10^{-4} Hz, the spectra are ordered according to the position in the pit and a steeper slope is observed, with an exponent varying from -1.93 ± 0.32 to -2.27 ± 0.18 (Fig. 9b). This part of the spectrum reflects the time variation of the outside temperature.

The value of the exponents in the 3×10^{-4} Hz to 4×10^{-3} Hz frequency range is not straightforward to interpret. However, qualitatively, heat exchange with the wall of the pit is described by a term $-(T - T_r)/\tau$ in the equation of the time evolution dT/dt of temperature. This term introduces a $1/f$ component in the frequency domain. If this term contributes significantly, the observed exponents thus would need to be increased by one unit in order to be compared with adiabatic RB conditions, giving a corrected exponent -1.6 in the upper part of the pit. This value is then close to the $-5/3$ exponent of KO scaling for a passive scalar. Spatial variations of exponents of temperature power spectra have also been reported in RB cells [54], and have been related to the nature of the coupling between temperature and velocity distributions. Note that, in our case, the dissipation frequency f_p, defined as the maximum of the power density spectrum $P(f)$ multiplied by f^2, is of the order of 5×10^{-3} Hz. It might be larger, as 5×10^{-3} Hz also corresponds to the frequency cut-off of the thermistors. In the frequency range below f_p, however, a scaling exponent -1.4 has been reported [22]. The frequency range where BO scaling (exponent $-11/5$) is observed in this RB experiment ($f > f_p$) is not accessible in our experiment.

In contrast with RB cell experiments, the temperature spectra in the pit do not exhibit any resonant frequency. In RB cells, coherent oscillations [20,21] appear at high Ra with a frequency f_R given by $\omega_R = 2\pi f_R = 0.36 - 0.5 Ra^{0.49} \kappa / h^2$. For $Ra = 10^{12}$, the expected oscillation frequency f_R is therefore 0.002–0.004 Hz, which lies in our measurement range at the edge of the cut-off of the response of the thermistors. Moreover, in the quarry pit, we would not expect a sharp peak because of the varying Ra conditions associated with varying outside temperature.

Further observations deserve to be pointed out concerning the exponents of the temperature power spectra. Indeed, significant differences are observed when considering different periods of time, with a systematic difference during the increasing phase of the air avalanches (for example the period from 15 to 20 December in Fig. 3) and during their decreasing phase (for example the period from 22 to 25 December). Such hysteresis effects may be significant features of this turbulent system, which could be related to seasonal variations of St mentioned before, but this needs to be investigated in more details.

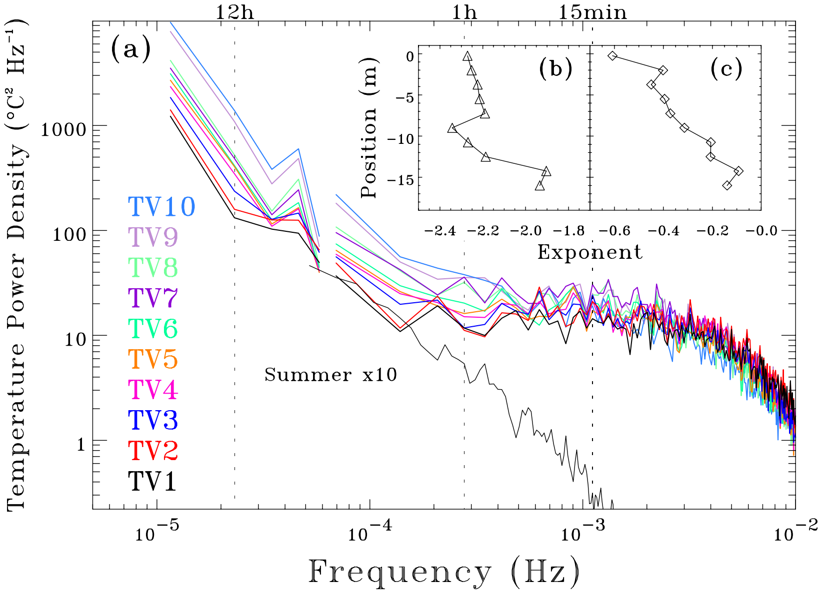

Fig. 9. (a) Temperature power density spectra for the vertical set-up using data recorded from 7 to 12 March 2004 (sampling 10 s). For frequency smaller than 6×10^{-5} Hz, spectra are averaged over portions of 24 hours and, for frequency larger than 7×10^{-5}, spectra are averaged over portions of 4 hours. The black line shows part of the power spectrum of TV1 in summer (August 2003), multiplied by 10 for convenience. Insets: Exponent of frequency variation of the temperature power spectrum versus position in the pit. The exponent is determined from 8×10^{-6} Hz to 8×10^{-5} Hz (b), and from 3×10^{-4} Hz to 4×10^{-3} Hz (c).

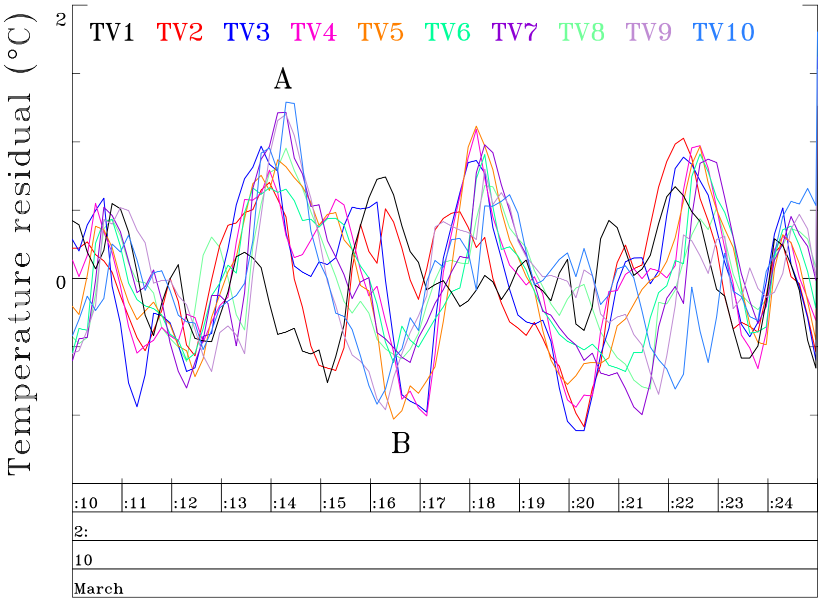

Fig. 10. Temperature time series recorded with the vertical profile TV1-10 on 10 March 2004 from 2:10 pm to 2:50 pm UT. Sampling interval is 10 s. Letters A and B refer to comments in the text.

6 Vertical correlations and estimates of velocities

Figure 10 displays the temperature time series in the high frequency range. Spatial coherence of the signals is striking on neighboring sensors. This observation is confirmed by the PDF (Fig. 11) of the correlation coefficients $C_{i,i+1}$ of neighbours TV$_i$ and TV$_{i+1}$. This correlation coefficient is defined over a sliding time interval of $2N+1$ data points as:

$$C_{i,\,i+1}(K) = \frac{\sum_{K-N}^{K+N} T_i(k) T_{i+1}(k)}{\sqrt{\sum_{K-N}^{K+N} T_i(k)^2}\sqrt{\sum_{K-N}^{K+N} T_{i+1}(k)^2}}, \tag{14}$$

where $T_i(k)$ refers to the residual temperature time series for sensor TVi, after subtraction of the mean value over this time interval of $2N+1$ data points. A value of $N=5$ is used here. The distributions shown in Figure 11 are strongly peaked near 1, with significantly smaller correlation coefficients for the last two pairs of sensors toward the top of the pit. Note that anti-correlations, although statistically less frequent, are not completely absent in this system.

In Figure 10, traveling waves can also be followed from sensor to sensor with definite delay times. For example, the peak labeled A can be followed from TV1 to TV10 with a time delay of 1 min, which corresponds to a velocity of 27 $\mathrm{cm\,s^{-1}}$. Sometimes the situation is more complicated. For example, in the peak labeled B in Figure 10, TV1-2 are anti-correlated to TV3-TV10. Although the order of magnitude of the velocity is large given our sampling time and the intrinsic cut-off response of the thermistors, it is interesting to attempt a systematic determination of velocity from the observed delay times.

Consider for example the distribution of delay times between sensors TV3 and TV6 on the one hand, and sensors TV3 and TV9 on the other hand. The delay time is obtained in the following fashion [23,55]. For each data point, the correlation coefficient between two sensors is computed using a portion of $2N+1$ data points (N previous points and N following points) as described by equation (14), with $N=5$. Then, the time series of the second sensor is shifted by one data point and the correlation is calculated again. The delay time corresponds to the time shift between the two series that maximizes the correlation. The distribution of the delay time t_{3-6} between TV3 and TV6 is peaked at 10 s, corresponding to one sampling interval. The distribution of the delay time t_{3-9} between TV3 and TV9 is wider and it has an average value of 14 s.

The obtained delay times can be used to infer a value of the velocity. This determination relies on Taylor's frozen flow assumption and has been extensively used in the context of RB flows [23,55]. For this purpose, we require the two delay times t_{3-6} and t_{3-9} to be of the same sign. A linear fit is then performed versus position to obtain a value of velocity. The distribution of velocity values consists in one sharp peak near zero and two wide distributions between 5 and 40 $\mathrm{cm\,s^{-1}}$ and between $-40\ \mathrm{cm\,s^{-1}}$ and $-5\ \mathrm{cm\,s^{-1}}$. The average value of the distribution above 5 $\mathrm{cm\,s^{-1}}$ is $23.1 \pm 0.1\ \mathrm{cm\,s^{-1}}$, with a standard deviation of 8.8 $\mathrm{cm\,s^{-1}}$. The average value of the distribution below $-5\ \mathrm{cm\,s^{-1}}$ is $-22.3\pm0.2\ \mathrm{cm\,s^{-1}}$, with a standard deviation of 8.7 $\mathrm{cm\,s^{-1}}$. These values can be compared with the estimate given above from the RB scaling laws (60 $\mathrm{cm\,s^{-1}}$), and with the estimate obtained from radon (2 $\mathrm{cm\,s^{-1}}$).

Another estimate can be obtained from dimensional arguments at the level of the flow restriction, namely the windows. The ventilation flow rate is then of the order of $A^*\sqrt{g\Delta T^*/T_K}$, where A^* is the effective area of the windows and ΔT^* is the temperature difference between the upper part of the pit and the outside atmosphere. Taking $A^* = S_w/2 = 1.1\ \mathrm{m^2}$ and $\Delta T^* = 5$ °C (the mean value corresponding to above estimates of velocities), the flow rate is 0.46 $\mathrm{m^3\,s^{-1}}$ which leads to a velocity of 6 $\mathrm{cm\,s^{-1}}$ in the pit. This value is intermediate between the estimate from radon and the estimate from the RB scaling law. The measured value is compatible with these estimates. Note however that the value 22 $\mathrm{cm\,s^{-1}}$ above cannot be considered as a typical average velocity. Indeed, the determination selects the correlated time portions with significant delay times. This tends to favor medium velocity values. Larger values will lead to delay times smaller than our time resolution. It is also likely that lower values of the velocity will yield signals that are not correlated properly between TV3 and TV9. Taylor's hypothesis also will not apply in the case of the slower waves.

A more significant feature of the velocity distribution is the fact that positive velocities are more frequent than negative velocities, with a ratio of 8700 to 3300. This indicates that along the vertical profile from TV3 to TV9, during the period of analysis (from 7 to 12 March 2004), upward motion was present 73% of the time. This observation is compatible with the geometry of the pit and the qualitative argument, derived previously from the skewness of the temperature distributions, of dominance of hot plumes in the lower part of the vertical set-up. Cold air avalanches fall on the side of the pit next to the windows, whereas hot avalanches travel preferably up the other side of the pit, as seen at least in the lower part of the vertical set-up (see shaded arrows in Fig. 1). This is however an averaged picture and the directions of motion can be reversed, in about 27% of the time. Turbulent behavior is expected in this change of pattern. With this picture in mind, the horizontal profile appears as a particularly interesting instrument.

7 Horizontal correlations and vorticity index

The PDFs of the correlation coefficients ${C^H}_{ij}$ between neighboring sensors i and j of the horizontal profile (BH1 to BH5) are shown in Figure 12. These distributions differ from the distributions of the correlation coefficients of neighboring sensors of the vertical profile displayed in Figure 11. Between BH1 and BH2, the correlation coefficient is largely positive and large. While moving towards the centre of the pit, from to BH1 to BH3, the value of the average neighbor correlation coefficient decreases ($0 < {C^H}_{23} < {C^H}_{12}$). Between BH3 and BH4, however, negative values of the correlation coefficient ${C^H}_{34}$ dominate. On the other side of the pit (BH4 and BH5), the correlation coefficient ${C^H}_{45}$ becomes positive again. Two regions can therefore be distinguished: sensors BH1-3 and sensors BH4-5. The horizontal profile, which roughly coincides with a diameter of the pit (Fig. 1), therefore shows the presence of a vertical shear zone between the turbulent flow of hot air from the quarry and the turbulent flow of cold air from outside.

This behavior can actually be noticed from the temperature time series. As indicated by the distribution of ${C^H}_{34}$ in Figure 12, most of the time, BH3 and BH4 exhibit opposite temperature fluctuations. The behavior of the correlation coefficients as a function of time (Fig. 13a) appears

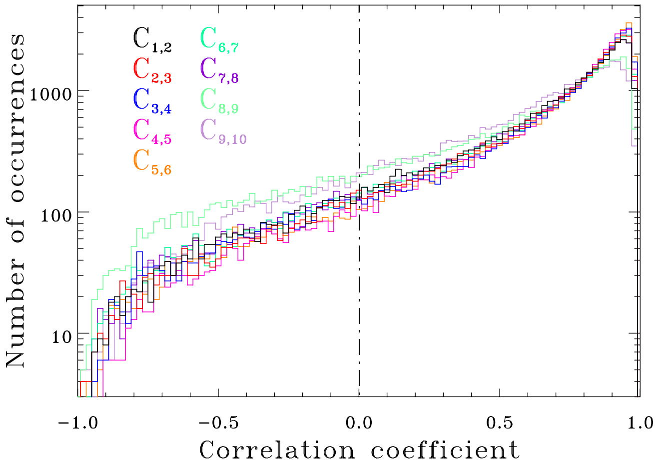

Fig. 11. Distribution of neighbor correlation coefficients obtained using temperatures recorded with the vertical set-up from 7 to 12 March 2003 (sampling 10 s). Correlations are determined using 100 s-long sliding portions.

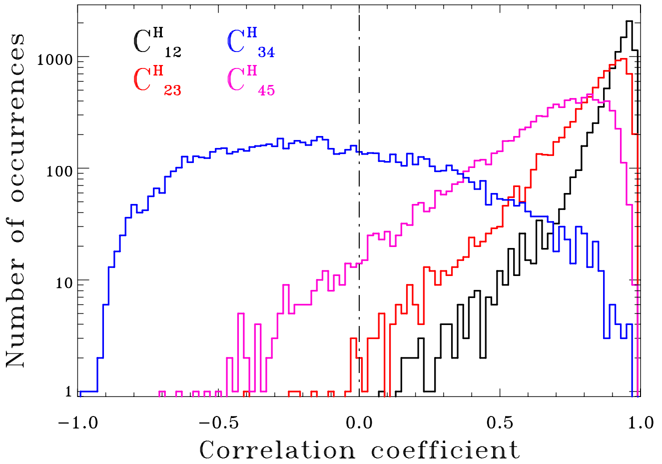

Fig. 12. Distribution of neighbor correlation coefficients obtained using temperatures recorded with the horizontal set-up from 21 to 27 March 2003 (sampling 1 min). Correlations are determined using 20 min-long sliding portions.

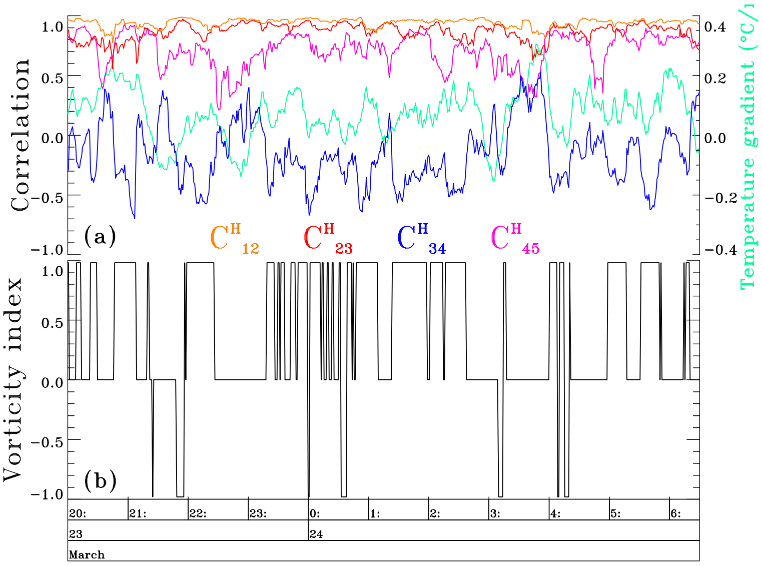

Fig. 13. (a) Neighbor correlation coefficients obtained using data of the horizontal set-up from 23 to 24 March 2003 (sampling 1 min) and temperature gradient along the horizontal set-up (green curve) (b) vorticity index. The length of the portion used to compute the correlation coefficient using equation (14) is $2N + 1 = 21$ data points. The temperature gradient is obtained from a linear fit of the temperature versus position on the horizontal profile.

particularly interesting, with sudden level changes reminiscent of the pattern of changes of wind directions [6], the reversals of the mean wind in the RB cell [23], or the pattern of the geomagnetic inversions [30]. In addition, positive correlations of $C^H{}_{34}$ are associated with decrease of the correlation coefficient $C^H{}_{12}$, suggesting bursts of large-scale loss of coherence over the horizontal profile. Such periods may correspond to transient motions of a different nature, such as a rotation around the vertical axis of the pit. Some abrupt variations of $C^H{}_{34}$ (1:30 a.m. and 2:15 a.m. on March 24) seem to be anticipated by a correlated smooth variation of $C^H{}_{34}$ and $C^H{}_{45}$, indicating possible precursory transition regimes. Precursory regimes, even when not systematic, may be of importance. For example, we may be currently in such a transition regime of the geomagnetic field [56].

Negative values of $C^H{}_{34}$ can be associated with a dominating shearing motion, a motion that can equivalently be referred to as vorticity around a horizontal axis. In addition to the correlation pattern, the values of the temperatures along the horizontal profile, themselves, define the polarity of this vorticity. Indeed, if the temperature is larger at sensor BH5, with an associated cold peak on sensor BH1, then it can be concluded that a burst of hot plumes rises on the right side of the profile whereas a burst of cold plumes falls on the left side (Fig. 1). This configuration is referred to as positive vorticity and the opposite one as negative vorticity of the motion. The sign of vorticity can be defined precisely by the sign of the temperature gradient fitted along the profile. This temperature gradient is also shown as a function of time in Figure 13a (green curve).

A vorticity index ξ is then constructed from ${C^H}_{34}$ and this temperature gradient. The vorticity index is considered to be zero if ${C^H}_{34}$ is larger than some threshold c_0. If ${C^H}_{34}$ is smaller than c_0, then the vorticity index is equal to ± 1, according to the sign of the temperature gradient. Here we take $c_0 = -0.2$. The vorticity index is shown in Figure 13b as a function of time. This variable encompasses both the time intervals without vorticity, with a remarkable pattern of resting at zero level, and the patterns of the polarity reversals. The time structure of the vorticity index can now be compared with the patterns of reversals of the LSC in RB cells.

The dynamics of the correlation coefficient ${C^H}_{34}$ and the vorticity index ξ can be studied in the frequency domain by Fourier transform $\hat{C}^H_{34}(\omega)$ and $\hat{\xi}(\omega)$, where $\omega = 2\pi f$. The corresponding power density spectra $|\hat{C}^H_{34}(\omega)|^2$ and $|\hat{\xi}(\omega)|^2$ are shown in Figure 14 as a function of frequency. For ${C^H}_{34}$, a power-law behavior is observed from 2×10^{-4} Hz to 10^{-2} Hz. The cut-off frequency f_c around 3×10^{-4} Hz is related to the duration t_C of the portion of $2N + 1$ data points used to compute the correlation coefficients (20 minutes here). A similar scale-free behavior for $f > f_c$ is observed for the vorticity index.

Power-laws of the form:

$$\left|\hat{C}^H_{34}(\omega)\right|^2 \propto f^{-a} \text{ and} \tag{15}$$

$$\left|\hat{\xi}(\omega)\right|^2 \propto f^{-b} \tag{16}$$

are fitted from 5×10^{-4} Hz to 8×10^{-3} Hz and yield values of the exponent $a = -2.1 \pm 0.1$ for ${C^H}_{34}$ and $b = -1.34 \pm 0.05$ for the vorticity index. As pointed out for the rotation index γ of the reversals of the LSC in RB cells [23], the value close to 2 of the exponent of $|\hat{C}^H_{34}(\omega)|^2$ may indicate a Brownian process. This value is also compatible with the $-11/5$ characteristic value of BO scaling. Our definition of the vorticity index depends on the parameter t_C. If this parameter is varied, the time series of the vorticity index and the frequency cut-off f_c are changed, but the value of the exponent remains unchanged.

The mean vorticity index over the period of time shown in Figure 13b is 0.08. This value is stable when the parameter t_C is changed, as long as it remains below one hour. Beyond one hour, the correlations between the signals are lost. The information about turbulence, as expected, is contained in the high frequency range of the temperature fluctuations ($f > 2 \times 10^{-4}$ Hz), and not in the low frequency temperature variations (Fig. 9).

Another way to capture the information contained in the time distribution of the vorticity index is to study the distribution of the quiescence intervals, defined as the duration of resting at vorticity index zero. This is similar to the alternative approach described in RB cells, when studying the distribution of time intervals between reversals [23]. Although the statistics is limited in this case, a power-law is suggested in the distribution of quiescence times over more than one order of magnitude of time, with an associated exponent of -1.2 ± 0.2. Such a value suggests a self-organized hierarchical phenomenon. The similarity with the pattern observed in RB cells is thus striking [23]. More work is needed however to assess the significance of this comparison.

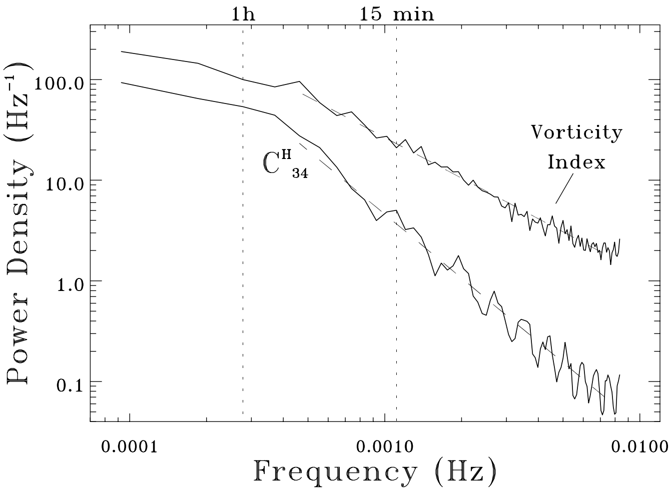

Fig. 14. Power density spectra of the vorticity index and of the correlation coefficient ${C^H}_{34}$ between BH3 and BH4. Dashed lines corresponds to power-law fits performed from 5×10^{-4} Hz to 8×10^{-3} Hz with slope $a = -2.1 \pm 0.1$ for the correlation coefficient ${C^H}_{34}$ and $b = -1.35 \pm 0.05$ for the vorticity index. The length of the portion used to compute the correlation coefficient using equation (14) and the vorticity index is $2N + 1 = 21$ data points.

Long-term variations of ${C^H}_{34}$ and of the vorticity index are shown in Figure 15b, together with the temperature time series of the horizontal profile (Fig. 15a). Again, bursts of anti-correlations are observed, with bursts of vorticity changes, with a positive or negative polarity preference varying over time. In addition to stochastic processes, the polarity of vorticity seems to be affected by external factors as well. Indeed, repeated negative polarity of vorticity are observed during the night and morning from 25 to 29 March, associated with a lower temperature on BH4 and BH5 compared with BH1-3. Before March 25, by contrast, the preferred polarity of vorticity is positive.

8 Discussion

In this paper, the spatial and temporal properties of the temperature field during regimes of air avalanches in a vertical quarry pit have been described. An interesting picture of a turbulent system emerges, with a nonhomogenous mixing state characterized by a reproducible and persistent spatial structure of the averaged properties. In addition, turbulent processes causing broad-band nearly Gaussian temperature fluctuations exhibit a temporal dynamics also characterized by scale-free statistics.

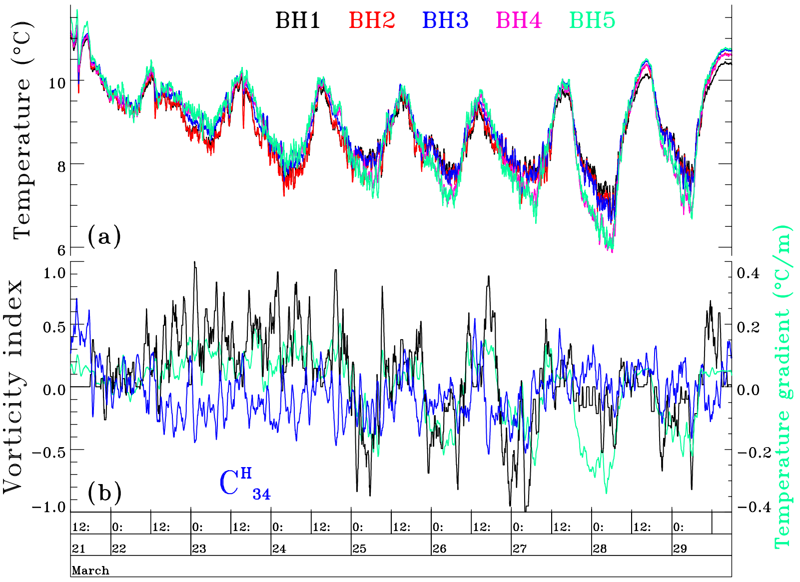

Fig. 15. (a) Temperatures recorded with the horizontal set-up from 21 to 29 March 2003 (sampling 1 min), averaged over 10 min-long sliding windows. (b) Correlation coefficient $C^{H}{}_{34}$ between BH3 and BH4 (blue curve), temperature gradient along the horizontal set-up (green curve) and vorticity index (black curve). These quantities are determined using $2N+1 = 21$ data points, and subsequently averaged over 2 hour-long sliding windows. The temperature gradient is obtained from a linear fit of the temperature versus position on the horizontal profile.

This is illustrated in particular by the behavior of the vorticity index, a variable constructed using the data of a horizontal temperature profile. The dynamical properties of the turbulent flows in the pit thus offer a rich area for investigations.

Consequences of the turbulent mixing properties observed in the pit for the energy and matter balance of the pit itself, and for the quarry as a whole, need to be considered. An estimate of the energy flux in the pit was given in Section 3. Another estimate can be obtained from the temperature profile writing:

$$F'_C = \rho c_p \frac{S_{\mathit{eff}}}{2} \Delta T' \, V, \tag{17}$$

where $\Delta T'$ is the mean temperature difference between BH1 and BH5. Taking $\Delta T'$=1 °C and $V = 2$ cm s^{-1}, we have $F'_C = 172$ W. This local estimate at the position of the horizontal profile is interesting to compare with the estimate $F_C = 333$ W (Sect. 3) obtained from the vertical profile and the upper limit $F^0_W = 235$ W of the heat exchange with the wall. The comparison between F'_C and F_C suggests that the absolute velocity could be larger at the level of the horizontal profile, or, alternatively, that the horizontal profile does not sample the full mean horizontal temperature gradient. The comparison between F_C and F^0_W suggests that only 29% of the heat flux is transmitted to the quarry, the rest being absorbed by the pit itself. These estimates however remain questionable. These two points, the role of the heat exchange with the wall to establish the equilibrium quasi-stationary state and the interplay of vertical and of mean horizontal air flows, will need to be analyzed in more details.

In order to discuss the nature of the turbulence observed in this system, expected turbulent scales can be estimated using classical scaling laws. The typical velocity V given by the volumetric flux estimated from the seasonal variation of the radon concentration, is 2 cm s^{-1}. This corresponds to $Re = VD/\nu = 6000$ and to a characteristic frequency $f_0 = V/2\pi h = 1.6 \times 10^{-4}$ Hz. Note that this frequency, which corresponds to the initial scale of turbulent fluctuations associated with the air avalanches, is compatible with the lower frequency limit of the broad band fluctuations in the power spectrum (Fig. 9a). The Kolmogorov frequency f_K, which defines the upper limit of the inertia domain, can be estimated [57] as $f_K = f_0 Re^{3/4} = 0.1$ Hz. This frequency corresponds to a spatial scale $\lambda_K = V/2\pi f_K = 3$ cm. Below λ_K, the energy of the turbulent cascade is dissipated by viscous friction. Note that both the frequency f_K and the scale λ_K lie outside our measurement domain.

The Bolgiano frequency f_B defines the lower limit of the so-called buoyancy subrange and the upper limit of the inertia subrange [22]. It can be estimated [22] as $f_B = V/2\pi\lambda_B$ where λ_B is the Bolgiano length given by $\lambda_B = hNu^{1/2}/(RaPr)^{1/4}$, where Pr is the Prandtl number ν/κ. Taking $Nu = 600$ and $Ra = 10^{12}$, gives $\lambda_B = 50$ cm and $f_B = 0.006$ Hz. Thus, our measurement range lies in the inertia subrange of turbulence. In this domain, it can be argued that the temperature fluctuations correspond predominantly to fluctuations of the mean velocity, rather than the background thermal turbulence [22].

Power spectra of the horizontal correlation $C^{H}{}_{34}$ and of the vorticity index indicate a scale-free character. This is an interesting observation at a scale which is intermediate between the laboratory scale [23] and the atmospheric scale of wind reversals [6]. Scale-free processes are ubiquitous in natural [8] and artificial systems. The values of the exponents, $a = -2.1 \pm 0.1$ for $C^H{}_{34}$ and $b = -1.34 \pm 0.05$ for the vorticity index (Eqs. (15) and (16)), remain to be interpreted. The value -2.1 lies between the exponent -2 of a pure Brownian process [8] and the $-11/5$ of BO scaling. Similarly, -1.4 could correspond to a fractional Brownian process [8], or could be related to the -1.35 exponent observed in RB experiments for the velocity spectrum in the inertia subrange [22].

The relationship between the physical properties of turbulence in the pit, and the properties of RB turbulent convection needs to be analyzed in more details. Buoyancy is the main driving force in the pit for reasonably constant atmospheric pressure conditions. One interesting question in this respect is whether the scaling properties of RB convection still hold, and under which conditions. Another important feature is common: the up-going and down-going motion and associated plumes have to share the same cylinder. This implies that quasi-stationary convection cells have to be established in both systems. Several configurations are possible and the configuration occupied at a given time can change. Nevertheless, in our case, more configurations are possible than in a RB cell, and, in addition, more frequent transitions between energetically equivalent configurations are expected. A particularly interesting phenomenon is the coupling between axial rotation and horizontal rotations. However, most of the RB convection experiments are performed at aspect ratios D/h larger than 0.5 [58], and few data are available at the low aspect ratio 0.23 of the Vincennes pit. To our knowledge, numerical simulations also have not investigated such low values of the aspect ratio.

While the comparison with RB cells is interesting, there are important intrinsic differences between the two systems. The geometry here is complicated, and there may be disturbances due to the presence of the staircase. The air humidity may also play an important role with respect to a normal thermal RB Boussinesq cell. These two effects however can be probably neglected for an idealized scenario. However, the free entrance at the top and the large quasi-stable reservoir represented by the quarry at the bottom change drastically the geometrical and possibly dynamical properties of the system. Qualitatively, the pit should include less re-circulations of the same fluid elements, and more fresh plumes. Typical lifetime of eddies should also be different in both cases, as well as the resulting large-scale turbulent diffusivity.

Thus, the quarry pit actually offers a realization of thermal convection in a quasi-constant temperature gradient without boundary layers, a situation referred to as homogeneous thermal convection [59]. This situation corresponds to unstably stratified turbulence, such as occurring in the central part of a RB cell, the so-called zone of bulk convection. Therefore, our system should rather be compared with the bulk part of RB convection. Up to now, this bulk convection has been investigated numerically only. In the study of Borue and Orszag [59], it has been shown that KO scaling holds in this case instead of BO scaling. Furthermore, in this calculation, it is observed that the LSC is formed by a few strong ascending/descending jets, whose appearance is prevented by the upper and lower boundary layers in a closed RB cell. This calculation thus could account rather well for the situation observed in our experiment. As mentioned above, while compatible with it (Sect. 5), we actually cannot distinguish KO scaling unambiguously because of the cut-off frequency and the contribution of heat exchange with the walls.

The regime of bulk turbulence is heuristic in the physics of turbulence. Indeed, a recent numerical study by Lohse and Toschi [60], expanding the scope of the Borue and Orszag calculation, has shown that if the boundary layers are suppressed by using periodic boundary conditions, the elusive ultimate Kraichnan regime of turbulence [61], characterized by Nu proportional to $Ra^{1/2}$, immediately follows. This ultimate regime could not be confirmed in recent classical RB experiments [23], but could be evidenced in one experiment using rough walls at top and bottom [62], which causes an artificial suppression of the boundary layers. The calculation by Lohse and Toschi [60] thus confirms the role of the boundary layers in preventing the appearance of the ultimate regime. Note that the ultimate regime, in this calculation, is forced by a mean linear temperature profile; this condition in our system results from the boundary temperatures of the external atmosphere and the equilibrium quarry temperature, smoothed by the heat exchange with the walls (see Fig. 6 and Sect. 4).

While it is premature to state that an equivalent of the ultimate Kraichnan regime is realized in the pit, our experiment may bring valuable clues on the physical nature of turbulence and the role of boundary layers in shaping the large scale flows. The quarry pit therefore appears as a novel medium scale model that may be of great value for the understanding and the application of the physics of turbulence in natural systems.

The authors thank Marc-André Delannoy, Michel Laroche from Inspection Générale des Carrières, and the city of Paris for the access to the Vincennes quarry. Bernard Castaing is thanked for enlightening discussions. This experiment was performed with the support of E. Pili from Cea/HES. The original version of the manuscript was greatly improved by the insightful comments of two anonymous reviewers. This work is IPGP contribution No 2065.

References

1. B.I. Shraiman, E.D. Siggia, Nature **405**, 639 (2000)
2. L.P. Kadanoff, Phys. Today **54**, 34 (2001)
3. J.H. Costello, J.R. Strickler, C. Marassé, G. Trager, R. Teller, A.J. Freise, Proc. Natl. Acad. Sci. U.S.A. **87**, 1648 (1990)
4. G.W. Wetherill, Ann. Rev. Astron. Astrophys. **18**, 77 (1988)
5. T.H. Hankins, J.S. Kern, J.C. Weatherall, J.A. Ellek, Nature **422**, 141 (2003)
6. E.V. Doorn, B. Dhruva, K.R. Sreenivasan, V. Cassella, Phys. Fluids **12**, 1529 (2000)

7. G. Falkovich, A. Fouxon, M.G. Stepanov, Nature **419**, 151 (2000)
8. D.L. Turcotte, *Fractals and chaos in geology and geophysics* (Cambridge University Press, Cambridge, England, 1992)
9. S. Braginsky, P. Roberts, Geophys. Astrophys. Fluid Dyn. **38**, 327 (1987)
10. E.M. Blanter, C. Narteau, M.G. Shnirman, J.-L. Le Mouël, Phys. Rev. E **59**, 5112 (1999)
11. C. Narteau, E. Blanter, J.-L. Le Mouël, Phys. Earth Planet. Int. **120**, 271 (2000)
12. T. Mikkelsen, H.E. Jorgensen, M. Nielsen, S. Ott, Boundary-Layer Meteorology **105**, 483 (2002)
13. J.H. Sorensen, D.K.J. Mackay, C.O. Jensen, A.I. Donaldson, Epidemiol. Infect. **124**, 577 (2000)
14. V.N. Goncharov, P. McKenty, S. Skupsky, R. Betti, R.L. McCrory, C. Cherfils-Clerouin, Phys. Plasmas **7**, 5118 (2000)
15. U. Frisch, *Turbulence: The legacy of AN Kolmogorov* (Cambridge University Press, Cambridge, England, 1995)
16. E. Villermaux, C. Innocenti, J. Fluid Mech. **393**, 123 (1999)
17. M. Zhang, T. Maxworthy, J. Fluid Mech. **470**, 247 (2002)
18. E.D. Siggia, Annu. Rev. Fluid Mech. **26**, 137 (1994)
19. R. Krishnamurti, D. Siggia, Proc. Natl. Acad. Sci. U.S.A. **78**, 1981 (1981)
20. B. Castaing, G. Gunaratne, F. Heslot, L. Kadanoff, A. Libchaber, S. Thomae, X.-Z. Wu, S. Zaleski, G. Zanetti, J. Fluid Mech **204**, 1 (1989)
21. X.L. Qiu, S.H. Yao, P. Tong, Phys. Rev. E **61**, R6075 (2000)
22. X.-D. Shang, K.-Q. Xia, Phys. Rev. E **64**, 065301(R) (2001)
23. K.R. Sreenivasan, A. Bershadskii, J.J. Niemela, Phys. Rev. E **65**, 056306 (2002); J.J. Niemela, L. Skrbek, K.R. Sreenivasan, R.J. Donnelly, Nature **404**, 837 (2000)
24. R. Verzicco, R.J. Camussi, Fluid Mech. **477**, 19 (2003)
25. X.-L. Qiu, P. Tong, Phys. Rev. E **64**, 036304 (2001)
26. X.-L. Qiu, P. Tong, Phys. Rev. E **66**, 026308 (2002)
27. X.-L. Qiu, X.-D. Shang, P. Tong, K.-Q. Xia, Phys. Fluids **16**, 412 (2004)
28. H.-D. Xi, S. Lam, K.-Q. Xia, J. Fluid Mech. **503**, 47 (2004)
29. U. Burr, W. Kinzelbach, A. Tsinober, Phys. Fluids **15**, 2313 (2003)
30. S.C. Cande, D.V. Kent, J. Geophys. Res. **100**, 6093 (1995)
31. Y. Gallet, V. Courtillot, Phys. Earth Planet. Int. **92**, 235 (1995)
32. R. Bolgiano, J. Geophys. Res. **64**, 2226 (1959); A.M. Obukhov, Dokl. Akad. Nauk. SSSR **125**, 1246 (1959)
33. A.N. Kolmogorov, Dokl. Akad. Nauk. SSSR **32**, 141 (1941)
34. X.-Z. Wu, L. Kadanoff, A. Libchaber, M. Sano, Phys. Rev. Lett. **64**, 2140 (1990)
35. S. Ashkenazi, V. Steinberg, Phys. Rev. Lett. **83**, 4760 (1999)
36. T. Mashiko, Y. Tsuji, T. Mizuno, M. Sano, Phys. Rev. E **69**, 0363065 (2004)
37. S. Grossman, D. Lohse, J. Fluid Mech. **407**, 27 (2000); S. Grossmann, D. Lohse, Phys. Rev. Lett. **86**, 3316 (2001); S. Grossman, D. Lohse, Phys. Rev. E **66**, 016305 (2002)
38. S. Grossmann, D. Lohse, J. Fluid Mech. **486**, 105 (2003)
39. F. Perrier, P. Morat, J.-L. Le Mouël, Phys. Rev. Lett. **89**, 134501 (2002)
40. F. Perrier, P. Richon, C. Crouzeix, P. Morat, J.-L. Le Mouël, J. Environmental Radioactivity **71**, 17 (2004)
41. D. Moiriat, D. Obert, P. Potherat, J. Bebien, M. Laroche, Bull. Inf. Bass. Paris **37**, 35 (2000)
42. C. Crouzeix, J.-L. Le Mouël, F. Perrier, P. Richon, P. Morat, C.R. Geoscience **335**, 345 (2003)
43. S. Brüggerhoff, G. Wange, P. Morat, J.-L. Le Mouël, F. Perrier, J. Cultural Heritage **2**, 117 (2001)
44. F. Perrier, P. Morat, J.-L. Le Mouël, Earth Planetary Science Letters **191**, 145 (2001)
45. T.M.L. Wigley, J. Geophys. Res. **72**, 3199 (1967)
46. X.-L. Qiu, K.-Q. Xia, Phys. Rev. E **58**, 486 (1998)
47. W.D. Baines, J.S. Turner, J. Fluid Mech. **37**, 51 (1969)
48. D. Gubbins, P. Kelly, Nature **365**, 829 (1993)
49. C. Laj, A. Mazaud, R. Weeks, M. Fuller, E. Herrero-Bervera, Nature **325**, 511 (1987)
50. G.A. Glatzmeier, R.S. Coe, L. Hongre, P.H. Roberts, Nature **401**, 885 (1999)
51. B. Mutlu Sumer, L.H.C. Chua, N.-S. Cheng, J. Fredsoe, J. Hydraulic Engineering **129**, 585 (2003)
52. K.-Q. Xia, S.-L. Lui, Phys. Rev. Lett. **79**, 5006 (1997)
53. R. Labbé, J.-F. Pinton, S. Fauve, J. Phys. II France **6**, 1099 (1996)
54. S.-Q. Zhou, K.-Q. Xia, Phys. Rev. Lett. **87**, 064501 (2001)
55. S.-Q. Zhou, K.-Q. Xia, Phys. Rev. E **63**, 046308 (2001)
56. G. Hulot, C. Eymin, B. Langlais, M. Mandea, N. Olsen, Nature **416**, 620 (2001)
57. L.D. Landau, E.M. Lifshitz, *Fluid Mechanics* (Pergamon Press, New York, 1953)
58. X.-Z. Wu, A. Libchaber, Phys. Rev. A **45**, 842 (1992)
59. V. Borue, S.A. Orszag, J. Sci. Comp. **12**, 305 (1997)
60. D. Lohse, F. Toschi, Phys. Rev. Lett. **90**, 034502 (2003)
61. R.H. Kraichnan, Phys. Fluids **5**, 1374 (1962)
62. P.E. Roche, B. Castaing, B. Chabaud, B. Hebral, Phys. Rev. E **63**, 045303 (2001)